

Biocasting of an Elastin-Like Recombinamer and Collagen Bi-Layered Model of the Vascular Wall

Received 00th January 20xx,
Accepted 00th January 20xx

Miguel González-Pérez,^a Dimitria Bonizol Camasão,^b Diego Mantovani,^b Matilde Alonso,^a and José Carlos Rodríguez-Cabello*^a

DOI: 10.1039/x0xx00000x

The development of vascular wall models will foster the development of preventive and therapeutic therapies for treating cardiovascular diseases. However, the physical and biological complexity of vascular tissue represents a major challenge, especially for the design and the production of off-the-shelf biomimetic vascular replicas. Herein, we report the development of a biocasting technique that can be used to replicate the tunica adventitia and the external elastic lamina of the vascular wall. Type I collagen embedded with neonatal human dermal fibroblast (HDFn) and an elastic click cross-linkable, cell-adhesive and protease-sensitive elastin-like recombinamer (ELR) hydrogel were investigated as layers to the envisaged model. Mechanical characterization confirmed that the viscous and elastic attributes predominated in the collagen and ELR layers, respectively. *In vitro* maturation confirmed the collagen and ELR cytocompatibility, while histology revealed the wavy and homogenous morphology of the ELR and collagen layer respectively, the cell polarization towards the cell-attachment sites encoded on the ELR, and the enhanced expression of glycosaminoglycan-rich extracellular matrix and differentiation of the embedded HDFn into myofibroblasts. As a complementary assay, 30 % by weight of the collagen layer was substituted with the ELR. This model proved the possibility to tune the composition and confirm the versatile character of the technology developed, while revealing no significant differences with respect to the original construct. On-demand modification of the model dimensions, number and composition of the layers, as well as the type and density of the seeded cells, can be further envisioned, thus suggesting that this bi-layered model may be a promising platform for the fabrication of biomimetic vascular wall models.

Introduction

Cardiovascular failure has the largest incidence worldwide among non-communicable diseases (NCDs). Indeed, whereas cancer, diabetes and chronic respiratory diseases together are estimated to be responsible for one third of NCD-related deaths in the elderly population (70 years and older), cardiovascular diseases alone account for 48 %¹, with approximately half of these conditions corresponding to coronary artery disease². This situation translates into an urgent need to develop biomimetic vascular models that provide the means to accelerate the investigation of novel therapies for cardiovascular complications from the laboratory bench³.

Although bioengineered vascular wall models have evolved to mimic the native vascular conduits⁴, imitate the proper biological clues, elastic behavior and ability to remodel and growth still remains a challenge⁵. The ubiquitous mechanical and biological behavior exhibited by the vascular wall is reflected in its layered composition⁶. Thus, the tunica intima encompasses a minimal basal lamina supported on a thin elastin layer known as the internal elastic lamina (IEL). The IEL lumen acts as the substrate for the anti-thrombogenic monolayer of endothelial cells (ECs) while preventing migration of the contractile smooth muscle cells (SMCs) distributed across the tunica media⁷. This collagen-based layer is further enclosed by

the external elastic lamina (EEL), which defines the beginning of the tunica adventitia, where fibroblasts (FBs), embedded in a collagen matrix, are found⁸.

Strategies inspired by the ability of vascular cells to express their own extracellular matrix (ECM) and form tissue sheets when cultured *in vitro* have been exploited to design tubular vascular wall models. In this sense, FB-expressing and devitalized tubular sheets have been wrapped with cellularized layers prepared from SMCs (tunica media)⁹, FBs (tunica adventitia)¹⁰ and both¹¹, and, in the latter two cases, subsequently lumenally coated with a monolayer of ECs. Although these models intimately reproduced the vascular wall structure and composition, their long manufacturing process (several months) represents a significant limitation for their production and study on a large scale.

Alternatively, use of ECM components, in combination with synthetic polymers, has been suggested to manufacture representative tubular models within a reasonable time. Thus, non-cellularized collagen and elastin models have been electrospun with crosslinking agents¹², poly(caprolactone) (PCL)¹³ or silk fibroin¹⁴, and cellularized collagen models have been cast and reinforced with Dacron^{15, 16} or substituted with photo-crosslinked gelatin¹⁷. Although these approaches afforded vascular-like structures, their lack of cells or need to substitute or add non-ECM proteins constitutes a major handicap as regards recapitulation of the vascular wall.

Herein we report a versatile approach for the manufacture of cellularized bi-layered elastin and collagen constructs as a model for the EEL and tunica adventitia. Neonatal human dermal fibroblasts (HDFn) were selected as the cell load for the collagen matrix of the bi-layered model envisaged. Their availability, inherent presence in the tunica adventitia and spatiotemporal remodelling activity on their host matrix¹⁸⁻²⁰

^a BIOFORGE (Group for Advanced Materials and Nanobiotechnology), CIBER-BBN, University of Valladolid, 47011 Valladolid, Spain.

^b Laboratory for Biomaterials and Bioengineering, Canada Research Chair I in Biomaterials and Bioengineering for the Innovation in Surgery, Department of Min-Met-Materials Engineering, Research Center of CHU de Québec, Division of Regenerative Medicine, Laval University, Québec, QC Canada G1V 0A6.

* Corresponding author.

Electronic Supplementary Information (ESI) available. See DOI: 10.1039/x0xx00000x

were considered to be appealing features for the intended vascular design. Isolated and reconstituted type I collagen was then chosen as the building block for the outer layer²¹. This protein offers intrinsic biodegradability²²⁻²⁴ and cell-interactive properties²⁵ while, as is the case for the tunica adventitia, working synergistically with the HDFn to enhance the mechanical response of the construct^{26, 27}.

Bioengineered elastin-like polypeptides based on the repetitive hydrophobic and elastic-conferring sequences of natural tropoelastin²⁸ were selected for the inner layer of the model. These recombinantly produced polypeptides, also known as elastin-like recombinamers (ELRs), preserve the native hydrophobic phase-transition and elastic recoil in water²⁹ while allowing the encoding and tethering of bioactive sequences such as cell-adhesive^{30, 31} and proteolytic sites^{32, 33}. In addition, physically^{34, 35} or covalently crosslinkable domains^{36, 37} can be incorporated into their backbone to guide the formation of tunable and stable hydrogels without requiring initiators or releasing potentially cytotoxic by-products during the manufacturing stage. In this light, an elastin layer comprising two ELR versions, namely RGD-ELR, which contains the cell-binding Arg-Gly-Asp tripeptide^{38, 39}, and GTAR-ELR, which bears the proteolytic Gly-Thr-Ala-Arg tetrapeptide from the urokinase plasminogen activator system (uPA enzyme)^{40, 41}, was chosen. In addition, in-situ click-crosslinkable domains were tethered to each ELR to provide a stable and elastic matrix when combined³⁷.

A bi-layered tubular model comprising an inner ELR and an outer HDFn-loaded collagen layer was produced upon subsequent addition of each component into a simple and versatile tubular mold. In addition, a model recapitulating the presence of elastin in the collagen-based tunica adventitia (30 % of ELR by weight) as well as a mono-layered ELR and collagen models as controls have been produced. Evolution of the viscoelastic properties, cell-mediated remodelling, in terms of matrix compaction and expression of ECM components, cell response and cell viability were examined after maturation *in vitro* for 3, 7 and 14 days.

Materials and methods

Cell culture

Neonatal human dermal fibroblasts (HDFn, C0045C, Gibco, Thermo Fisher Scientific, Waltham, MA, USA) were cultured in Dulbecco's Modified Eagle Medium (DMEM, Gibco) supplemented with 10 % fetal bovine serum (FBS, Gibco), 1 % Penicillin-Streptomycin solution (Pen-Strep, Gibco), 5 µg/mL human insulin (Santa Cruz Biotechnology, Dallas, TX, USA), 2 ng/mL Fibroblast Growth Factor-basic (FGFb, Gibco) and 0.5 ng/mL Epidermal Growth Factor (EGF, Invitrogen, Thermo Fisher Scientific) at 37 °C in a humidified atmosphere under constant 5 % CO₂. The experiments were performed with passages between 8 and 10.

Fabrication of the mono- and bi-layered ELR-collagen model

The two ELRs, namely RGD and GTAR, were expressed in *E. coli* bacteria and functionalized with azide and cyclooctyne groups, respectively. DNA recombinant techniques, bioproduction, modification, purification and characterization are described in detail elsewhere^{32, 42, 43}. Type I collagen was extracted from rat tail tendons, sterilized and processed according to a reported protocol²¹. A 1:1 mixture (v/v) of the click-modified ELRs dissolved at 40 mg/mL in phosphate buffered saline (PBS) at 4 °C was prepared and poured directly (1 mL) into a custom-made 48 multiwell plate (Corning REF 353078, Corning, NY, USA) containing a polypropylene mandrel in the center (Ø = 3.8 mm; Figure 1A). The plate was kept at 4 °C for 40 minutes and then at 37 °C for 40 minutes, thus allowing time for click crosslinking of the ELR chains in their solvated state³⁷ while ensuring the subsequent phase transition of the ELR-hydrogel, respectively (Figure 1B). The hydrogel was gently detached from the well to obtain the ELR mono-layered model (Figure 1C). For the ELR mono-layered model, the expelled PBS was replaced with growth factor-free culture medium (DMEM supplemented with 10 % FBS and 1 % Pen-Strep, hereafter referred to as DMEM+) (Figure 1D), whereas for the bi-layered models, the PBS phase was immediately substituted by the outer HDFn-cellularized collagen-based layer.

The second layer was prepared containing either 0 % (Figure 1E) or 30 % of the ELR (%w/w) in collagen (Figure 1F). Thus, click-complementary ELRs were mixed in a 1:1 proportion (v/v) at 4 mg/mL in PBS at 4 °C and added directly, in the desired proportion (0 % and 30 % ELR %w/w), to a type I collagen solution prepared at 4 mg/mL in 0.02 N acetic acid. This solution was mixed with a neutralizing buffer solution (3.5× DMEM supplemented with 10 mM HEPES and 60 mM NaOH) and a suspension of HDFn (at 6 × 10⁶ cells/mL) in DMEM+ in a 2:1:1 proportion, respectively. A volume of 0.91 mL (2 mg protein/mL, pH 7.2 and HDFn density of 1.5 × 10⁶ cells/mL) was poured around the ELR layer contained in the custom-made 48 multiwell plate and kept at room temperature (r.t.) for 30 minutes to form the outer collagen layer. The hydrogel formed was gently detached from the wall and DMEM+ medium was added to fill the well (Figure 1G and 1H), thus obtaining the bi-layered models referred to as ELR-Col and ELR-Col70%ELR30%, respectively. Physical interactions may be established between the collagen and ELR layers during this stage. As described previously⁴⁴, direct and water-mediated hydrogen-bonding interactions can arise between the peptide bonds and side groups present in both protein-based scaffolds, thereby triggering integration of the layers.

The same volume of the solution used to prepare the 0 % ELR (%w/w) outer collagen layer (0.91 mL) was poured into the custom-made 48 multiwell plate (containing a Ø = 3.8 mm mandrel in the center) and kept at r.t. for 30 minutes (Figure 1I). Subsequently, the hydrogel formed was detached from the well and covered with DMEM+, thus giving the Col mono-layered model (Figure 1J).

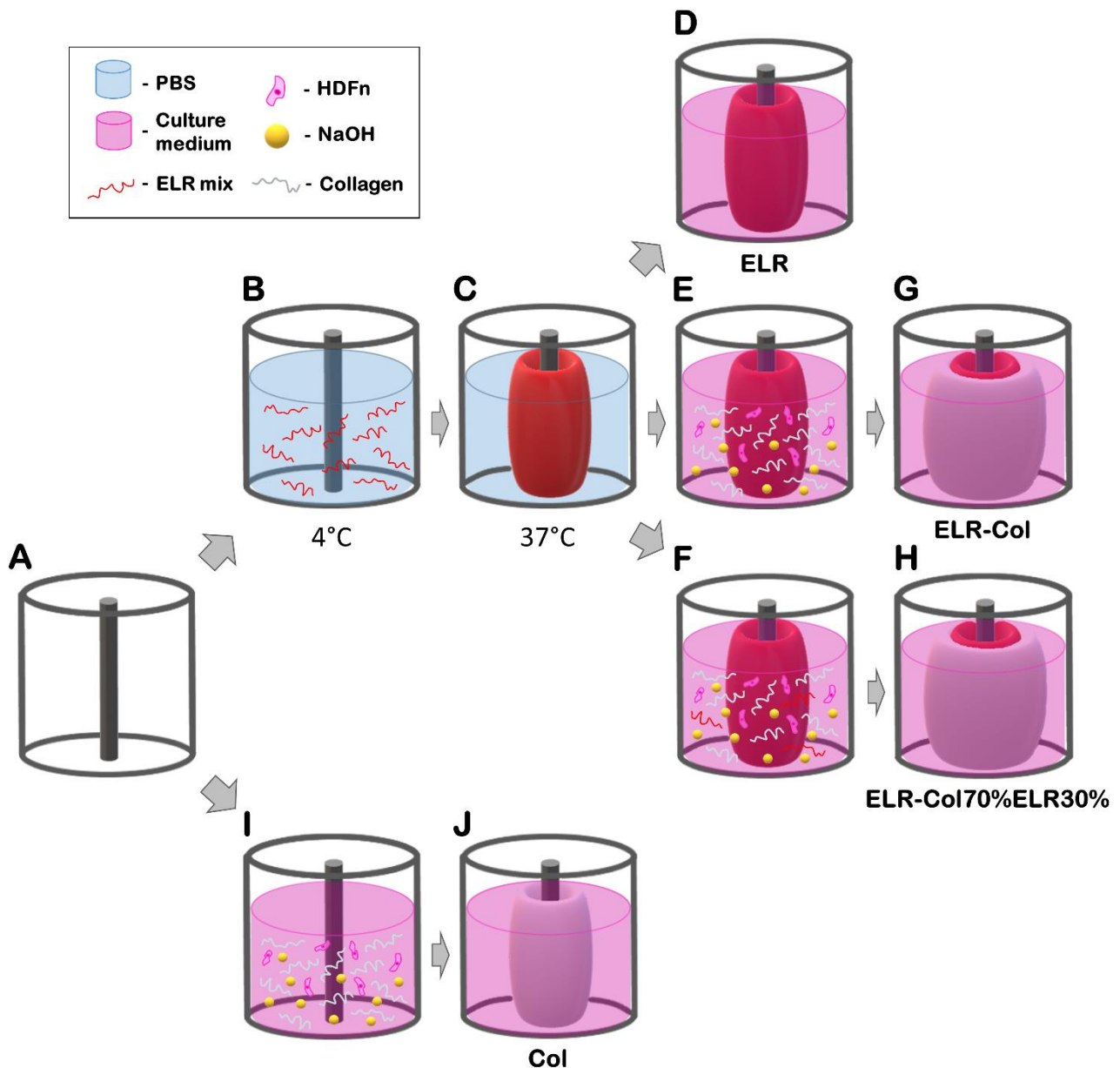


Figure 1. Schematic representation of the steps followed to manufacture the mono- and bi-layered models. Custom-made 48 multiwell plate containing a mandrel ($\varnothing = 3.8$ mm) in the center (A). Steps followed to prepare the ELR (B-C-D), ELR-Col (B-C-E-G), ELR-Col70%ELR30% (B-C-F-H) and Col (B-I-J). PBS: phosphate buffered saline; ELR: 1:1 mixture (v/v) of the click-modified RGD and GTAR; ELR-col: type I reconstituted collagen; HDFn: neonatal human dermal fibroblasts; NaOH: sodium hydroxide.

The mono- and bi-layered ELR, Col, ELR-Col and ELR-Col70%ELR30% models were matured at 37 °C and 5 % CO₂ for 3, 7 and 14 days, during which time the ELR and collagen layers acquired a reddish and whitish color, respectively. Four replicas, consisting of two samples for each condition and time point, were employed for the study. The culture medium was changed every two days.

Macroscopic characterization

A Leica DMS1000 B TL5000 microscope (Leica Biosystems, Wetzlar, Germany) was used to visualize the macroscopic evolution of the mono- and bi-layered models on days 3, 7 and 14 during maturation *in vitro*.

Histology: Histochemistry and immunohistochemistry

The biocast models were rinsed in PBS and fixed in 3.7 % formaldehyde (Sigma-Aldrich, St Louis, MO, USA) at r.t. for 1 hour. Samples were dehydrated and soaked in paraffin using an automatized tissue processor (Tissue-Tek VIP, Sakura, Torrance, CA, USA) prior to block-paraffin embedding and cutting into circumferential cross sections with a thickness of 5 μ m using a rotary microtome (Leica RM 2125 RTS, Leica Biosystems). Slices were deparaffinised with xylene and rehydrated by successive washing with ethanol in deionized water at decreasing concentrations (100 %, 95 %, 80 %, 70 % and 0 %). For histological characterization, a modified Verhoeff Van Gieson Elastic Stain Kit (HT25A, Sigma-Aldrich), Papanicolaou's solution

1a Harris hematoxylin (1.09253, Sigma Aldrich) and eosin Y solution (318906, Sigma Aldrich) were used according to standard protocols. In addition, Alcian blue 8GX (A5268, Sigma Aldrich) solution in acetic acid was employed to examine the polysaccharides content. For immunohistochemistry, slices were rinsed three times in PBS 1X, permeabilized with 0.1 % TritonTM X-100, introduced in a humidified chamber and incubated for 1 h at r.t. in 5 % bovine serum albumin (BSA). Subsequently, slices were rinse twice (PBS 1X) and incubated individually with anti- α -smooth muscle actin (anti- α -SMA, A5228, 1:400, Sigma Aldrich) and anti-focal adhesion kinase (anti-FAK, SAB4502498, 1:400, Sigma Aldrich) in 1 % BSA (in PBS 1X) at 4 °C overnight. Slices were subsequently rinsed three times with PBS 1X and incubated with goat anti-mouse IgG H&L conjugated to Alexa Fluor 568 (ab175473, 1:500, Abcam) and goat anti-rabbit IgG H&L conjugated to Alexa Fluor 488 (ab150077, 1:500, Abcam) secondary antibodies in 0.2 % BSA (in PBS 1X) for 2 h at r.t., respectively. Fluoroshield Mounting Medium with DAPI (ab104139, Abcam) was used to counterstain the samples from immunostaining prior to observation. Images were acquired using a Nikon Eclipse 80i microscope and an inverted Nikon Eclipse Ti-E epifluorescence microscope coupled to a DS-2MBWc camera, using the NIS-Elements AR software package (Nikon Corporation, Minato, Tokyo, Japan). The distribution of cells in the cellularized collagen layer of the Col, ELR-Col and ELR-Col70%ELR30% models was evaluated quantitatively by selecting three randomly chosen internal, middle and external areas of the hematoxylin and eosin (H/E) stained samples.

Compaction characterization

As previously reported⁴⁵, contraction of the tubular models was evaluated by measuring the length with a caliper and the external and internal diameters with a scanning laser interferometer (LaserMike 136, Series 183B, NDC Technologies, Dayton, OH, USA). The mean and standard error of the mean for four different experiments are shown.

Cellular metabolic activity

The metabolic activity of the cellularized models was evaluated using the AlamarBlue Cell Viability assay (Thermo Fisher Scientific). Thus, culture medium was removed at the selected time points (3, 7 and 14 days) and replaced with 0.8 mL of resazurin solution in DMEM (1:10). After incubation at 37 °C and 5 % CO₂ for 4 hours, HDFn reduced the resazurin to fluorescent resorufin by aerobic respiration, thus allowing the metabolic activity to be measured. A multi-well plate spectrophotometer (Bio-Rad Model 450, Mississauga, ON, Canada) was employed to measure the fluorescence ($\lambda_{\text{ex}} = 560 \text{ nm}$; $\lambda_{\text{em}} = 590 \text{ nm}$) normalizing the obtained values against the Col model at day 3 for each condition. The mean and standard error of the mean for four different experiments are shown.

Mechanical characterization

The biocast models were mechanically characterized using an Instron E1000 (Instron Corporation, Norwood, MA, USA) equipped with a 5 N load cell. In order to approximate the measurement conditions to a physiological environment, ring-shaped samples with a length of 4-5 mm were immersed in PBS

at 37 °C and conditioned to a 5 % circumferential strain with the help of two custom-made L-shape grips. The strain value (ϵ) was calculated as follows (Equation 1):

$$\epsilon = \frac{l-l_0}{D_i\pi/2} \quad (\text{Eq. 1})$$

where $l-l_0$ corresponds to the gap between the positions after mounting the specimen at zero force (l_0) and once the load has been applied (l), and $D_i\pi/2$ corresponds to half the circumference of the sample, i.e. D_i represents the internal diameter. From the applied 5 % strain, five progressive stress-relaxation cycles, each consisting of 10 % strain ramps (5 %/s strain rate) and 600 seconds of relaxation at constant strain, were performed. Once the last cycle (55 % strain) was complete, a uniaxial test to failure was performed at a 5 %/s strain rate. The coefficient between the measured force and the initial cross-sectional area of the sample defined the stress (σ) (Equation 2):

$$\sigma = \frac{\text{Measured force}}{2 \cdot (\text{Thickness}) \cdot (\text{Width})} \quad (\text{Eq. 2})$$

Elongation and stress values up to 45 % strain, were fitted to the Maxwell-Wiechert model (Equation 3)⁴⁶ using MATLAB (MathWorks, Natick, MA, USA), thus providing the initial (E_0) and equilibrium elastic modulus (E_E) for the biocast models:

$$\sigma(t) = \epsilon_0 E_E + \epsilon_0 E_1 \cdot \exp\left(-\frac{t}{\tau_1}\right) + \epsilon_0 E_2 \cdot \exp\left(-\frac{t}{\tau_2}\right) \quad (\text{Eq. 3})$$

Herein, the stress at a given time in each relaxation cycle is represented by $\sigma(t)$, the applied strain by ϵ_0 , the elastic components by E_i and the relaxation times by $\tau_i = \eta_i/E_i$ ($i = 1$ and 2). The initial elastic modulus (E_0) results from the sum of E_1 , E_2 and E_E , while the test to failure determines the corresponding tensile strength and strain at break. The mean and standard error of the mean for four different experiments are shown.

Statistical analysis

GraphPad Prism 7 (GraphPad software, La Jolla, CA, USA) was employed to compare the gathered data using a two-way ANOVA with post-hoc Tukey test (level of significance of 0.05). Statistical significance was represented with the following code: ns $p > 0.05$; * $p \leq 0.05$ and ** $p < 0.001$.

Results

Manufacture of mono- and bi-layered models: Biocasting technique

Mono- and bi-layered models imitating the EEL and tunica adventitia of the vascular wall^{47, 48} have been fabricated by sequentially combining an ELR and an HDFn-cellularized collagen solution using a biocasting technique. The use of a cylindrical container (48 multiwell plate) with a mandrel in the central position ($\emptyset = 3.8 \text{ mm}$) served as the tubular mold. Preliminary designs for the mold involving the use of one or two tubular pieces between the mandrel and the wall of the well were investigated to fabricate the bi-layered model. However, these preliminary approaches increased the number of steps and sample handling in detriment to the sterility and reproducibility of the technique. Indeed, the inherent ability of the ELR to hydrophobically fold in response to a change in temperature⁴⁹, and the ability of the collagen to self-assemble

and remodel upon embedding with cells^{20, 50}, made use of the tubular pieces dispensable. As such, the gelation time was optimized for each layer, thus ensuring the integrity of the crosslinked ELR matrix prior to the addition of the external collagen layer and manufacture of the bi-layered model.

As detailed, the ELR solution was added to the tubular mold first and then left at 4 °C for 40 minutes to allow homogeneous gelation of the solvated and unfolded ELR chains (Figure 1B). The mold was then heated to 37 °C for 40 minutes, thus inducing the phase transition and favoring detachment of the ELR hydrogel from the well prior to the addition of the HDFn-cellularized collagen (Figure 1C). The expelled solvent (PBS) was removed and the second HDFn-cellularized layer, containing 0 % or 30 % ELR (% w/w) in collagen, was injected directly (Figure 1E-F). The mold was kept at r.t. for 30 minutes to allow the gelation of the collagen layer and formation of the bi-layered model (Figure 1G-H).

As seen in the macroscopic view, the mono-layered ELR model exhibited an intense orange to red color, whereas a whitish appearance prevailed for Col over time (Figure 2A-B). In addition, a wavy morphology was observed for the ELR, which contrasts with the smooth appearance displayed by Col. Manipulation of these mono-layered models further evidenced their different mechanical properties, showing that Col sections

(≈ 3 mm height) were unable to remain in a vertical position at the studied time points (Figure 2B).

The morphological features displayed by the mono-layered models remained unaffected upon fabrication of the bi-layered ELR-Col (Figure 2C), with a reddish and undulating pattern being observed for the inner ELR layer and a whitish and homogenous layer for the outer collagen. No differences were noted when substituting 30 % of collagen for ELR (ELR-Col70%ELR30%), finding a similar morphology, color and ability to remain vertical for both bi-layered models (Figure 2C-D).

Histology

Cross sections of the models stained with the Elastic Stain Kit allowed the morphology and compaction of the mono- and bi-layered models upon maturation *in vitro* to be examined in greater detail with time (Figure 3).

The ELR model showed an irregular wavy pattern that experimented a slight reduction in wall thickness with time (Figure 3A). On the other hand, a homogeneous disc that progressively decreased in thickness was found for Col (Figure 3B). These layers appeared detached in the bi-layered models, with a thinner thickness being observed for the collagen layer than for the mono-layered Col at the time points studied (Figure 3C-D).

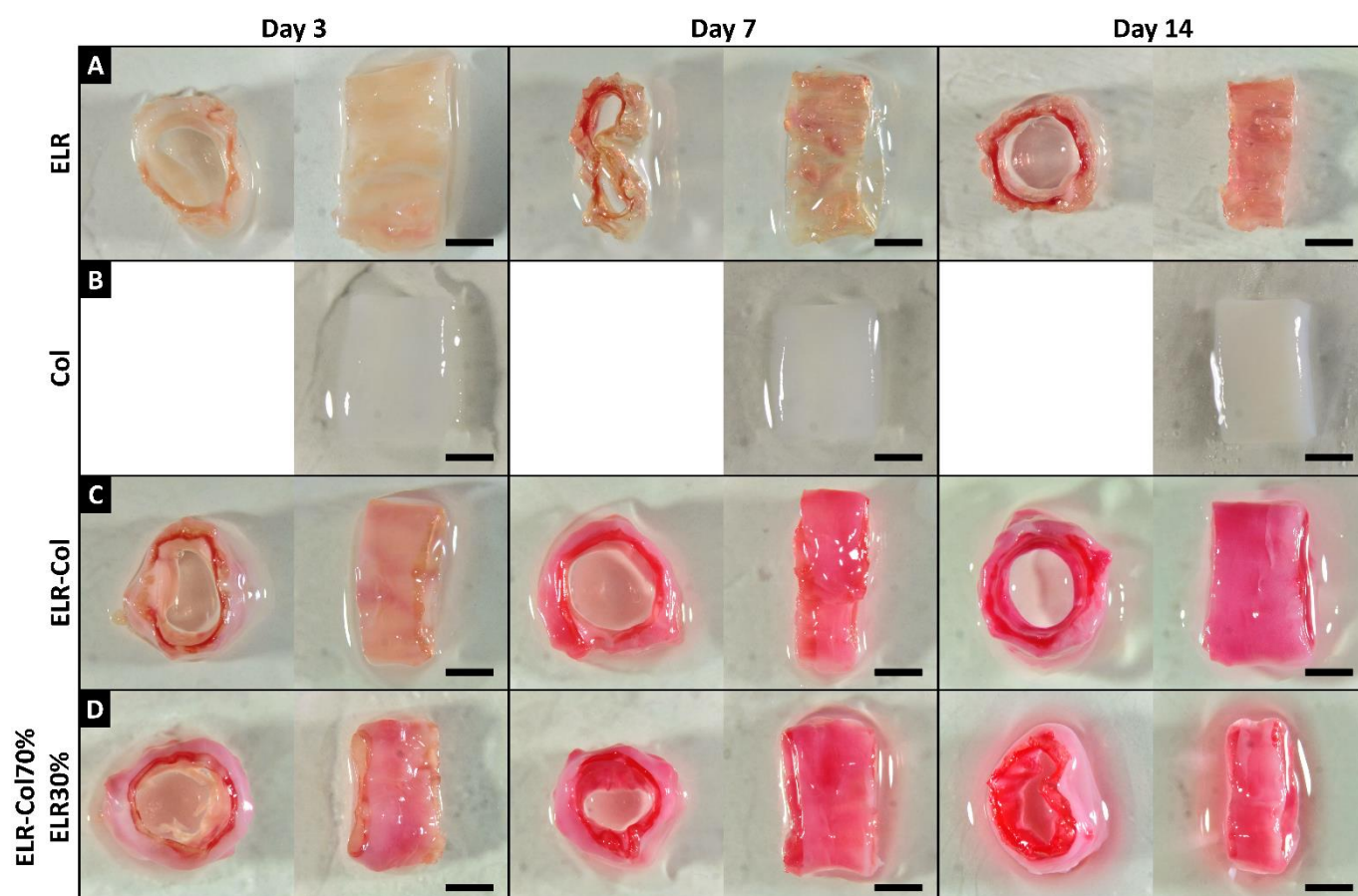


Figure 2. Macroscopic view of the biocast mono- and bi-layered models. Except for the Col models, which are unable to stand vertical, representative top and side views of the (A) ELR, (B) Col, (C) ELR-Col and (D) ELR-Col70%ELR30% at days 3, 7 and 14 are shown in each column. Scale bar: 2 mm.

Compaction and HDFn metabolic activity

The dimensions of the fabricated models allowed the evaluation of the compaction with time. ELR showed twice the residual volume when compared to Col at day 3 ($p < 0.001$, Figure 4A). This difference was maintained over time, with a slight

compaction being observed for both mono-layered models at days 7 and 14. A drastic reduction in initial volume was also observed for ELR-Col at day 3 (Figure 4A). This bi-layered model reproduced the trend reported for ELR and Col, showing a slight decrease and stabilization of the residual volume at days 7 and 14, respectively (Figure 4A).

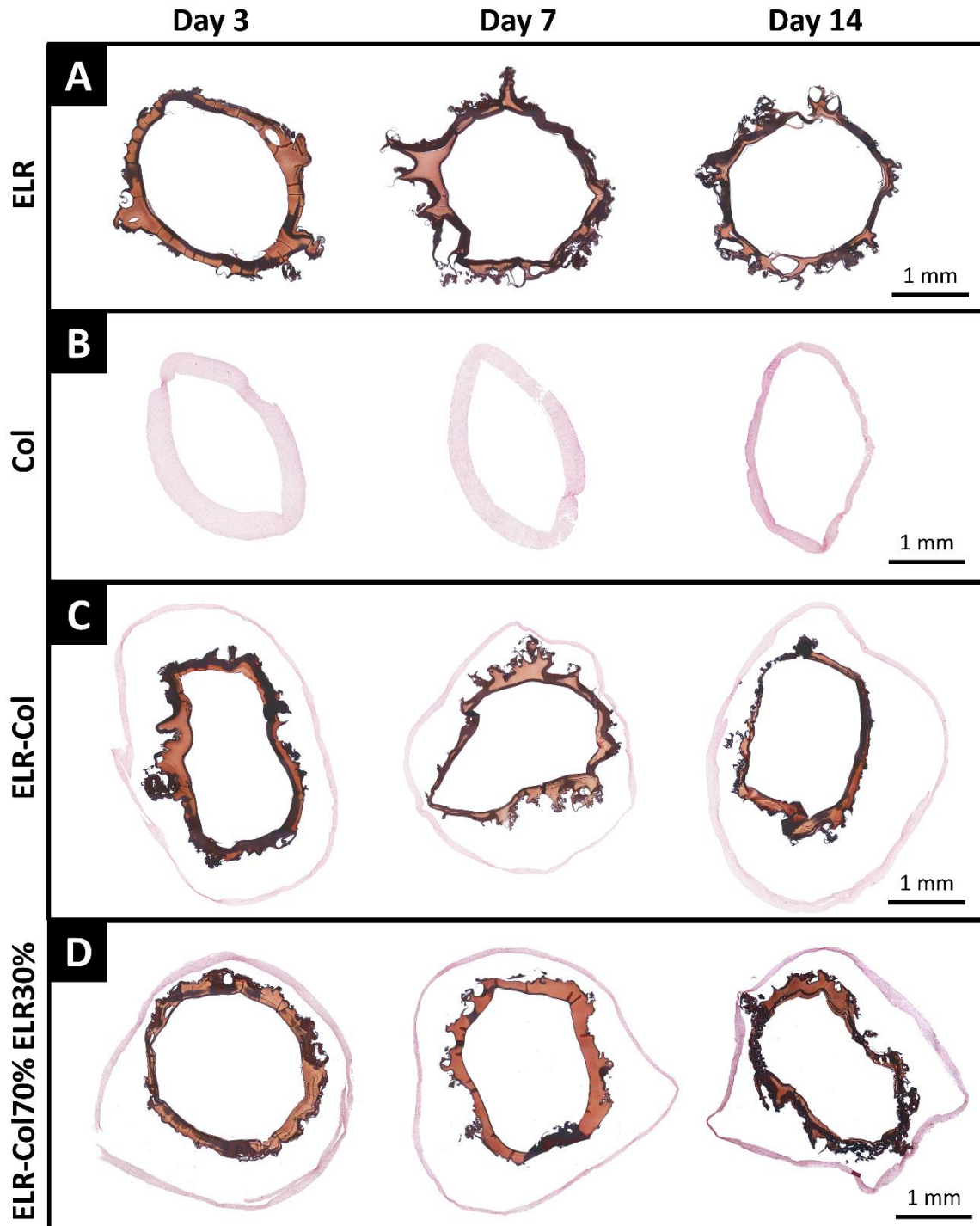


Figure 3. Evolution of the ELR and collagen layers in the mono- and bi-layered models upon maturation *in vitro* for two weeks. Representative images of (A) ELR, (B) Col, (C) ELR-Col and (D) ELR-Col70%ELR30% stained with the elastic stain kit at days 3, 7 and 14.

The 30 % substitution of collagen for ELR resulted in a slight higher compaction, with no significant differences at day 3 ($p > 0.05$, Figure 4A). Nevertheless, this effect approximated the ELR-Col70%ELR30% residual volume to that of Col ($p > 0.05$), with the significant difference observed between Col and ELR-Col disappearing at the time points studied ($p \leq 0.05$).

Splitting the residual volume into residual length and wall thickness further contrasted the behavior of the ELR and collagen matrix in these models. Figure 4B shows a marked reduction in the length of the Col model when compared to ELR ($p < 0.001$). However, this gap was not replicated for the wall thickness (Figure 4C), with no significant differences being found between ELR and Col ($p > 0.05$). As suggested in previous studies^{51, 52}, Col exhibits a stronger compaction in the cross section than in the longitudinal direction, with this effect also being observed for the ELR model but to a lesser extent. The bi-layered models studied reproduced the response displayed by ELR ($p > 0.05$), whereas the opposite effect was observed when compared with Col (at least $p \leq 0.05$).

The cytocompatibility of the ELR-Col model was then evaluated using the Col model as control, since this property has been

extensively studied for cellularized collagen gels⁵³. As seen in Figure 4D, although a slight reduction in metabolic activity was observed for ELR-Col at day 3, no significant differences were found at the time points studied ($p > 0.05$). This response was replicated by ELR-Col70%ELR30% confirming that the collagen matrix and the click-crosslinked ELR provide an appropriate environment for *in vitro* maturation of the embedded HDFn^{32, 36}.

Mechanical characterization: Elastic modulus

Circumferential tensile stress-relaxation tests were performed to determine the mechanical response of the models. The initial (E_0) and equilibrium (E_E) elastic moduli were obtained immediately after application of the load and at the end of the relaxation process respectively, allowing the short- and long-term response of the models to the subjected strain to be evaluated.

At day 3, the ELR exhibited an equilibrium elastic modulus (E_E) three times higher than that for Col ($p < 0.001$), thus revealing the higher mechanical response of the ELR matrix. Nevertheless, this difference decreased from $p < 0.001$ to $p > 0.05$ after maturation *in vitro* for two weeks (Figure 5A).

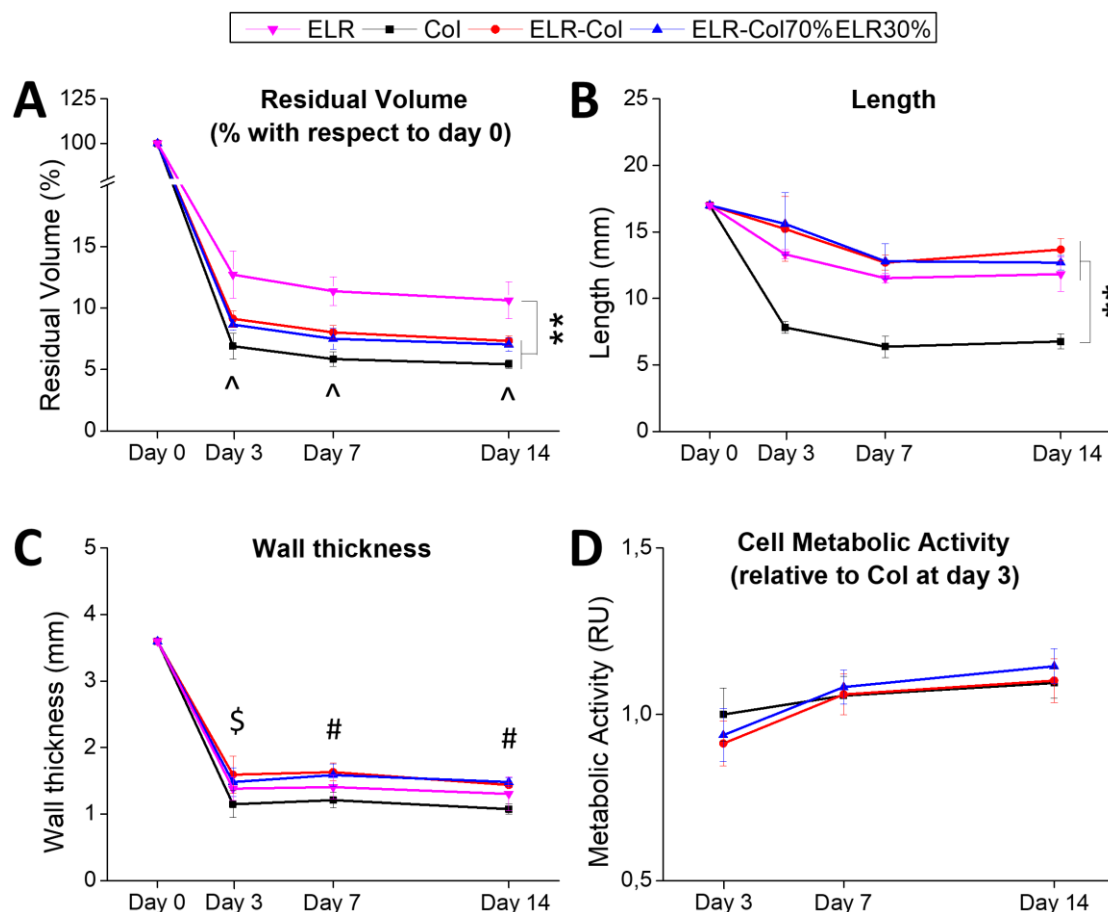


Figure 4. Evolution in the dimensions of the mono- and bi-layered models accompanied by the metabolic activity of the HDFn upon maturation *in vitro* for two weeks. (A) Residual volume (% with respect to day 0), (B) length and (C) wall thickness of ELR, Col, ELR-Col and ELR-Col70%ELR30% at days 3, 7 and 14. (D) Cell metabolic activity of HDFn embedded in the collagen layer of Col, ELR-Col and ELR-Col70%ELR30% (relative to Col at day 3) measured using the AlamarBlue assay at days 3, 7 and 14. ($n=4$, $\wedge p \leq 0.05$ for ELR-Col vs Col; $\$ p \leq 0.05$ for ELR-Col vs Col; $\# p \leq 0.05$ for ELR-Col and ELR-Col70%ELR30% vs Col; $p > 0.05$ was found for the comparisons not represented in the graphs). ** stands for $p < 0.001$.

No statistically significant differences between ELR-Col and ELR model were found at any time point ($p > 0.05$), whereas the opposite result was found for Col ($p < 0.001$). ELR-Col70%ELR30% replicated the behavior displayed by ELR-Col ($p > 0.05$), thus showing the predominant effect of the inner ELR layer over the mechanical response in the bi-layered models (Figure 5A).

As seen in Figure 5B, no significant differences were found between the E_0 values of the mono-layered models ($p > 0.05$), with a progressive increase being observed for Col with time (Figure 5B). This increase was reproduced in the bi-layered models, with ELR-Col and ELR-Col70%ELR30% being found to be essentially indistinguishable at the time points studied ($p > 0.05$).

The coefficient between the equilibrium and initial elastic modulus (E_E/E_0) evidenced the higher elasticity displayed by ELR when compared to Col ($p < 0.001$). Despite this, whereas the E_E/E_0 ratio remained virtually unaltered for ELR, exhibiting a 6 % increase after two weeks, a 23 % increase was found for Col (Figure 5C). ELR-Col replicated the E_E/E_0 ratio exhibited by the ELR, and also reproduced the increase observed for Col at day 14 (Figure 5C). Similarly, partial substitution of the collagen

layer for 30 % ELR by weight (ELR-Col70%ELR30%) resulted in essentially the same E_E/E_0 evolution and range of values as found for ELR-Col ($p > 0.05$).

Mechanical characterization: Tensile strength and strain at break

A circumferential uniaxial test to failure allowed the tensile strength and strain at break for the models to be determined at days 3, 7 and 14.

For ELR, a progressive increase in tensile strength at break was observed with time (Figure 5D), differing significantly from Col at days 7 and 14 ($p \leq 0.05$). The ELR response and range of values was replicated by ELR-Col, with no significant differences being found over time ($p > 0.05$). Substitution of 30 % of the collagen layer for ELR by weight resulted in a slight but statistically insignificant increase after two weeks ($p > 0.05$), thereby corroborating the dominating character of the ELR layer over the strength at break of the bi-layered models.

Figure 5E shows strain at break values seven times larger for ELR than for Col at days 3, 7 and 14 ($p < 0.001$). As for the strength at break, bi-layered ELR-Col and ELR-Col70%ELR30% preserved the behavior displayed by the ELR ($p > 0.05$), thus reproducing a slight increase and stabilization of the elongation at break values over time.

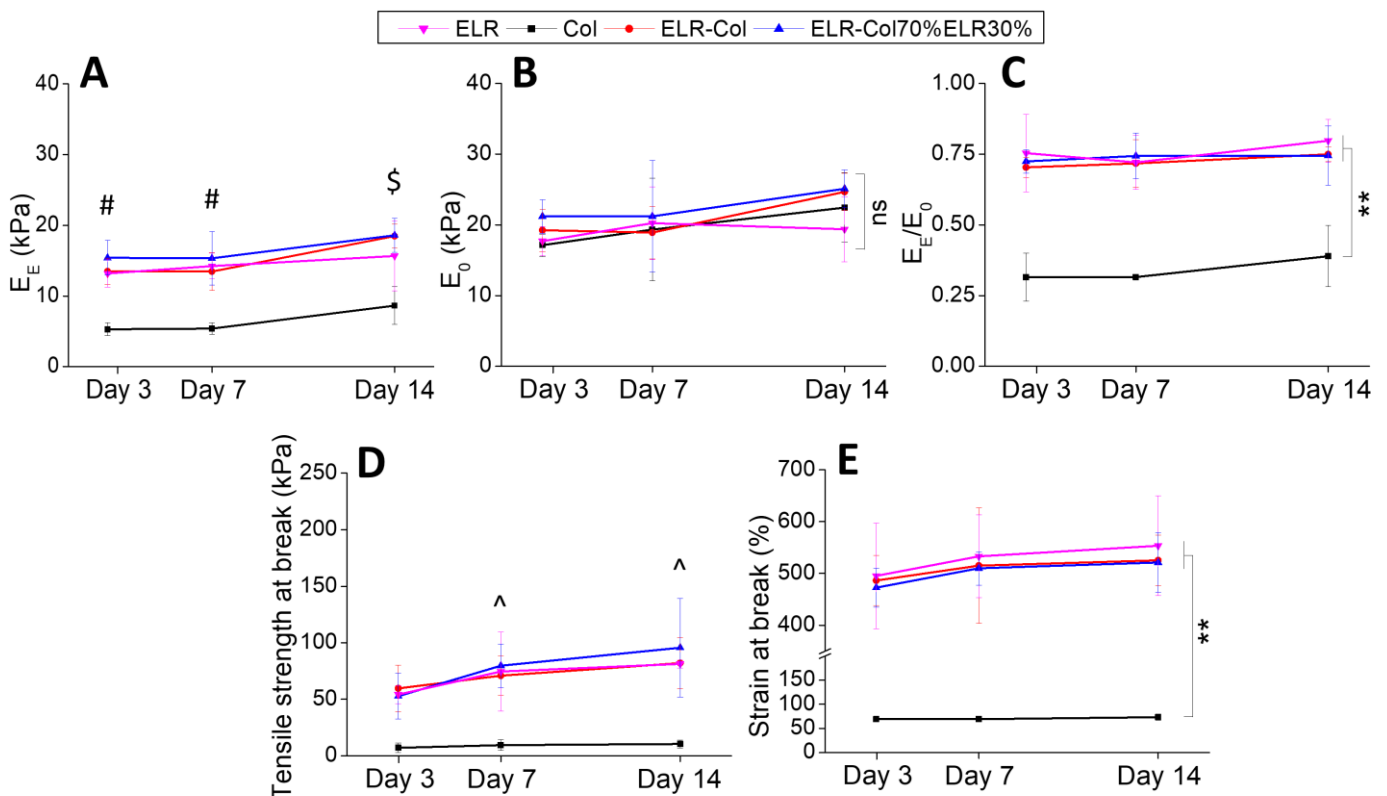


Figure 5. Evolution of the mechanical properties displayed by the mono- and bi-layered models measured by performing a circumferential tensile stress-relaxation and uniaxial tensile test to failure upon maturation *in vitro* for two weeks. (A) Tensile equilibrium elastic modulus (E_E), (B) tensile initial elastic modulus (E_0), (C) E_E/E_0 ratio, (D) tensile strength and (E) tensile strain at break for ELR, Col, ELR-Col and ELR-Col70%ELR30% at days 3, 7 and 14. ($n=4$, # $p < 0.001$ for ELR, ELR-Col and ELR-Col70%ELR30% vs Col; \$ $p \leq 0.05$ for ELR and $p < 0.001$ for ELR-Col and ELR-Col70%ELR30% vs Col; ^ $p \leq 0.05$ for ELR, ELR-Col and ELR-Col70%ELR30% vs Col; ns $p > 0.05$ was found for the comparisons not represented in the graphs). ** stands for $p < 0.001$.

Histochemistry and immunohistochemistry

H/E staining confirmed the progressive contraction observed for Col and revealed HDFn polarization towards the external surface in contact with the culture medium with time (Figure 6A). Significant differences between the number of cells in the external and internal regions of this model were found at day 3 ($p \leq 0.05$), with this polarization becoming more pronounced at days 7 and 14 ($p < 0.001$, ESI, Figure ES1). In contrast, the cells contained in the collagen layer of the bi-layered models exhibited a preferential distribution towards the internal surface in contact with the ELR (Figure 6A). Again, statistically significant differences were found between the external and internal regions of the collagen matrix at days 3, 7 and 14 ($p < 0.001$).

Alcian blue staining showed the presence of sulfated glucose-amino-glycan-rich extracellular matrix^{54, 55} in the collagen matrix of Col and the bi-layered models, and supported the observed polarization towards the external and internal surfaces, respectively (Figure 6B).

Immunofluorescence suggested the presence of α -SMA and FAK in Col at day 3, and further revealed the observed cell polarization towards the external surface at days 7 and 14 (Figure 6C-D). α -SMA and FAK were also detected in the cellularized collagen layer in the ELR-Col and ELR-Col70%ELR30% models at days 3, 7 and 14 (Figure 6C-D). In addition, as reported by H/E staining, cells showed a preferential arrangement towards the internal surface in contact with the ELR layer.

Discussion

A versatile biocasting technique for the manufacture of tubular bi-layered models replicating the EEL and tunica adventitia of the vascular wall is reported herein. Specifically, HDFn, ELR and collagen proteinaceous scaffolds have been explored, thus replicating the native composition and structure of the vascular wall in a reproducible and reduced time period of around 2 hours.

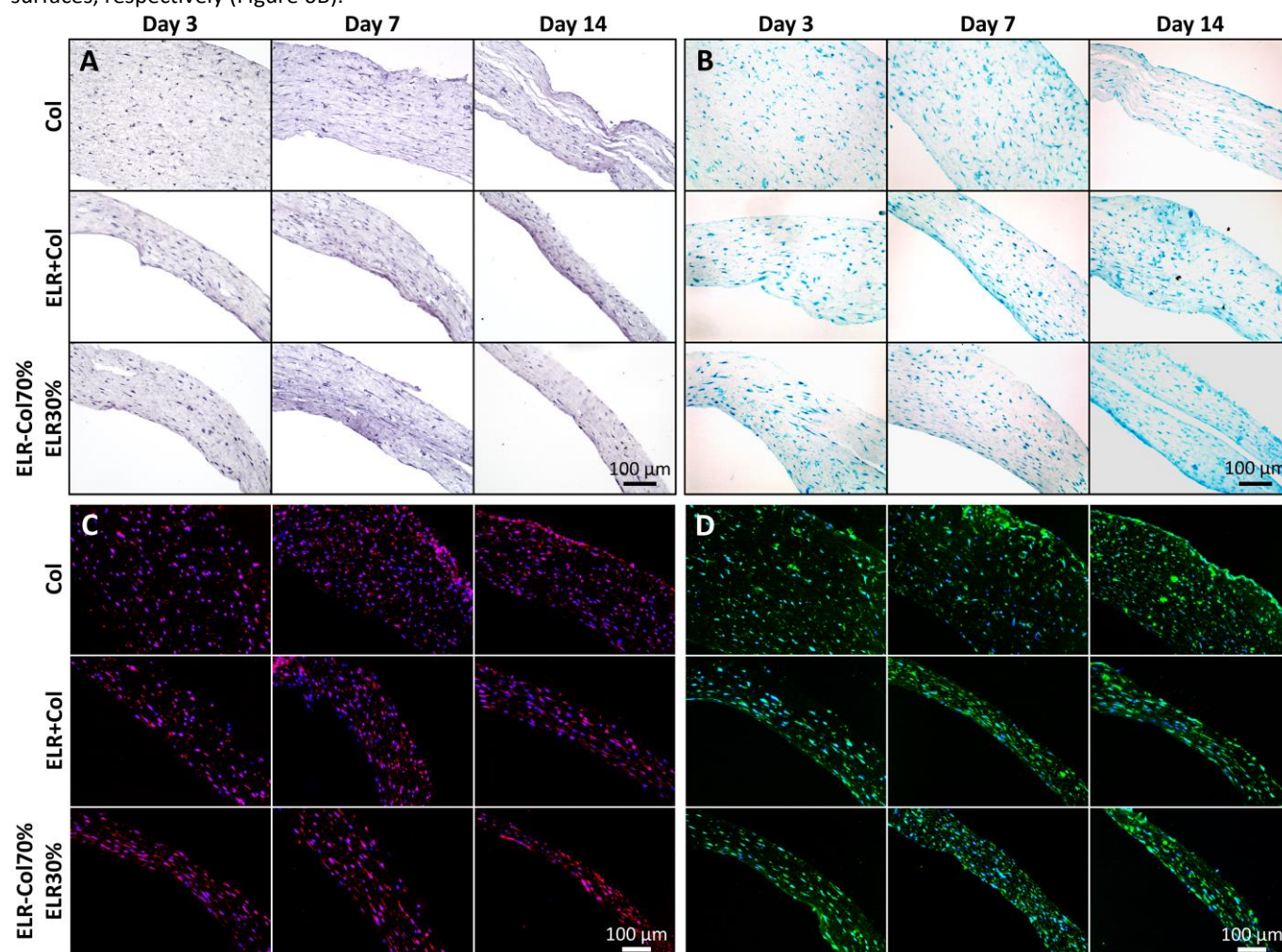


Figure 6. Evolution of cells, polysaccharides, α -SMA and FAK in the cellularized collagen layer upon maturation *in vitro* for two weeks. Representative images of the HDFn embedded collagen matrix for Col, ELR-Col and ELR-Col70%ELR30% stained with (A) hematoxylin and eosin, (B) Alcian blue, (C) α -SMA and DAPI, and (D) FAK and DAPI at days 3, 7 and 14. The left side of the section corresponds to the internal surface of the cellularized collagen layer in contact with the mandrel (Col) or ELR layer (ELR-Col and ELR-Col70%ELR30%), whereas the right side corresponds to the external surface in contact with the culture medium.

In addition to the simplicity and efficiency of the manufacturing process, the reported technique offers the possibility to adjust some of the parameters of the sample, such as the length, internal and external diameter, composition of the layers, and the cell type and density. Indeed, these features vary extensively along the vascular tree⁵⁶, thus suggesting that the technique developed herein may be a suitable approach for the design and manufacture of specific vascular wall models on demand.

The designed bi-layered model, referred to as ELR-Col, has a physiological-like appearance (Figure 2C). This finding can be related to the hydrophobic and hydrophilic character of the ELR and collagen matrix employed, respectively. The hydrophobic phase transition occurring between the ELR chains may tightly compact the ELR matrix⁵⁷, thus resulting in the undulating EEL morphology^{6, 7} and intensifying red color, presumably due to absorption of phenol red from the culture medium with time (Figure 2C). In contrast, the hydrophilic character and hydrogen-bonding interactions governing self-assembly of the collagen matrix^{58, 59} may produce the observed homogeneous pattern, thus imitating the smooth tunica adventitia instead^{6, 7}. Substitution of 30 % of the collagen for ELR by weight was found to be insufficient to confer a red color on the collagen layer while preserving the macroscopic features displayed by the original model (Figure 2D).

Histological characterization offered a better view of the matrix morphology of the ELR and collagen layers during maturation *in vitro* for two weeks. Wavy and fenestrated conformations became more evident in the ELR layer of the mono- and bi-layered models over time (Figure 3A,C-D). This pattern, which is characteristic of the internal and external elastic laminae⁶, arises due to the bioinspired composition of the ELR, thus conferring a native morphogenetic response upon maturation in the biological incubator (37 °C and 5 % CO₂). As described previously⁴⁷, this conformation contributes to the mechanical response of the vascular wall, providing the elastic fibers with the ability to extend and store strain during the cyclic loading and unloading stages. As mentioned above, the compaction observed for the cross sections appears to arise from the hydrophobically folded state of the ELR chains at 37 °C, which favors progressive aggregation of the ELR chains in the crosslinked matrix^{49, 60}.

In contrast, the collagen layer exhibits a smooth conformation accompanied by a pronounced volume compaction over time (Figure 3B-D). This morphology resembles the native appearance of the tunica media and adventitia⁶¹, whereas the progressive reduction in volume was assigned to HDFn cell attachment and remodeling activity over time^{20, 62}. As described previously^{63, 64}, the arrangement of collagen fibers is highly sensitive to the presence of cells and, in this regard, the embedded HDFn cells in this system are thought to exert traction forces that compact the protein chains in the short term^{65, 66}. Whereas, the presumed packed and matured state of the collagen fibrils may prevent enzymatic degradation while favoring ECM deposition with time⁶⁷.

Histological characterization shed further light on the integration between the two layers in the designed models. Although a number of non-covalent interactions may be established between the ELR and collagen layers⁴⁴, they are unable to preserve the integrity of the construct once subjected to the automatized tissue processing step. This treatment, which comprises several washings in EtOH/aqueous phases, toluene, and melted paraffin may influence the ELR and collagen matrix differently, thereby provoking the delamination between layers prior to microtome cutting and staining (Figure 3). As reported previously⁶⁸, a synergic interplay between chemistry (covalent and non-covalent interactions), topology and mechanics is required to achieve strong interfacial adhesion. Although traditional approaches, such as surface modification or the incorporation of artificial adhesives, can be considered as an effective solution, is not ideal as regards biomimicry of the vascular wall. Instead, cohesion of the collagen and ELR chains should be addressed at a molecular level. One possibility may involve reducing the ELR crosslinking time, thus facilitating penetration of the collagen molecules and inter-layer integration at the interface. Alternatively, topological adhesion technologies involving pH-responsive polymer coatings between the layers⁶⁹ may serve to interconnect the proteinaceous networks at the molecular scale. Here, the reconstituted collagen solution can be used in the same way, serving as a liquid coating at acid pH that diffuse and entangle the ELR and collagen layer as the pH equilibrates and gelation takes place. In addition, the unreacted click domains exposed on the ELR layer surface can be further exploited as anchoring sites for the collagen. The use of azidoproline-substituted⁷⁰ or click catalyst-free conjugated collagens⁷¹ may provide a powerful covalent crosslinking approach, thereby strengthening the interfacial adhesion and overall cohesion of the biocast models.

Mechanical characterization by way of circumferential stress-relaxation cycles, followed by a uniaxial test to failure, allowed the response of the designed models to be evaluated under similar vasodilation and constriction events to those experimented in the vascular wall⁷². As can be seen, ELR-Col showed an equilibrium elastic modulus (E_E) resulting from a combination of the behaviors exhibited by ELR and Col individually (Figure 5A). Thus, the ELR layer may confer high E_E values as a result of the crosslinked and hydrophobically coiled chains²⁹. In contrast, *in vitro* maturation of the collagen-embedded cells may exert cohesive and alignment forces on the collagen fibers⁶⁴ as they progressively express their own ECM^{73, 74} reinforcing the mechanical properties at day 14. Similarly, this response was replicated for the E_0 and E_E/E_0 values (Figure 5B-C), further revealing the reduced viscous and predominantly elastic behavior of ELR-Col⁷⁵. Indeed, the intrinsic elasticity of the elastin protein plays a key role in the vascular wall. During loading cycles, the elastic fibers share the increased blood pressure with the relatively stiff collagen by undergoing a deformation in the circumferential direction. At this point, the elastic fibers permit the accumulation of strain while preventing slippage of the collagen. Tension is released at the end of each

pulse, thus resulting in recovery of the wall morphology and preparing the conduit for the following loading stage^{76, 77}.

As reported for the elastic moduli, the contribution of the ELR layer prevailed over the ELR-Col in terms of tensile strength and strain at break (Figure 5D-E). This response corroborated the inherent ability of the crosslinked and hydrophobically assembled ELR matrix to elongate and store energy while delaying the failure of the model with increasing strain. As such, the ELR layer may assist the outer collagen during the uniaxial test, thus explaining the slight reduction in the strain at break seen upon comparison with the mono-layered ELR (Figure 5E). This observation appears to be supported by collagen-based models where lower elongation at break values have been reported⁷⁴.

Interestingly, the ELR-Col70%ELR30% model showed no significant differences in terms of E_E , E_0 , tensile strength and strain at break when compared with ELR-Col ($p > 0.05$). This result confirms the versatile nature of the technique developed as regards selection of the ELR composition of the outer layer, up to a 30 %, without compromising the mechanical response. This ability can be further envisaged for addressing the reduced elastogenesis achieved by cellularized collagen-based models^{64, 73, 78}, biomimicking the vascular elastic fibers and approaching the native physiology⁷.

As found, the mechanical properties displayed by the designed bi-layered model differ markedly from those reported for the native coronary artery (elastic modulus and strength at break values of the order of 1.4 MPa)⁷⁹⁻⁸¹. The ECM in vascular walls, which mainly comprises mature collagen and elastic fibers, appears to display a tightly organized and aligned structure along with cells, namely ECs, SMCs and FBs⁶. This synergic arrangement provides the unique mechanical behavior of the vascular wall, thus preventing a direct comparison between our bi-layered model and the native tissue. Selection of the cell type and cell density may be a powerful tool for modulating the mechanical properties of the model developed herein. According to related studies found in the literature, the substitution of HDFn for SMCs should induce a stronger compaction of the collagen matrix⁶⁴, while a higher cell density can complement this effect by intensifying ECM expression and matrix remodeling in a shorter maturation time⁸². Both these modifications may result in reinforcement and approximation to the vascular wall mechanics in an elegant and controlled fashion.

In contrast, the ELR-Col and ELR-Col70%ELR30% models withstood elongations at break ten times larger than the native coronary artery (ca. 54 %)⁸⁰. Indeed, these models further exceeded the strain at break exhibited by the elastic fibers of ligaments (≈ 200 %)⁸³. The presence of microfibrils intertwined with the elastin⁸⁴, along with the accompanying cells, collagen and the thin conformation found for the internal and external elastic laminae⁶, seems to compromise the extensibility of the native tissue, thus resulting in the large difference found with the bi-layered models manufactured herein.

The ELR layer not only serves for reproducing the commonly overlooked ELL⁸⁵⁻⁸⁷ but also offers a tailorable scaffold for including bioactive domains able to modulate the cell behavior

towards a physiological-like vascular wall model. Here, embedded HDF appear to respond to the cell-adhesive and proteolytic sites encoded in the ELR matrix. As described previously⁵¹, the impaired diffusion of oxygen and nutrients from the culture medium to the internal surface of the collagen matrix can trigger cell polarization towards the external surface of Col (ESI, Figure ES1). Nevertheless, this tendency appears to be counteracted in the bi-layered models, where the cell-adhesive clues encoded in the ELR layer reverse this polarization, thereby stimulating migration towards the vicinity of the ELR-Col interface. Moreover, the protease-sensitive sequences included in the ELR matrix can also be considered to be promoters of the cell polarization observed. However, no signs of cells penetrating the ELR layer were found (ESI, Figure ES2) proving that degradation and cell-infiltration of the ELR matrix during the time studied is negligible. This result is in accordance with previous studies³², in which a period of three weeks was required to trigger enzymatic digestion of an ELR matrix implanted subcutaneously in mice. In addition, fibroblast cells have also been shown to maintain an activated state during maturation *in vitro* for two weeks⁷⁴, thus suggesting a preferential expression of ECM components and reduced biodegradable activity that preserves the protease-sensitive ELR layer.

This hypothesis was supported by Alcian blue staining, which revealed the presence of acid (carboxylated and sulphated) polysaccharides in the cellularized collagen layer of the mono- and bi-layered models (Figure 6B)⁸⁸. These molecules, which conform the glycosaminoglycans (GAGs) and proteoglycans (PGs) responsible for cell attachment and migration in the ECM^{89, 90}, are abundantly produced and focally secreted by the HDF when behaving as myofibroblasts⁹¹. These cells, which are characteristic of wound-healing processes⁹², display contractile⁹³, adhesive⁹⁴, mechanosensory⁹⁵ and migratory properties⁹⁶ as a result of their active expression of α -SMA and FAK, amongst others. As can be seen in Figure 6C and 7D, both components were detected in the collagen layer of the Col, ELR-Col and ELR-Col70%ELR30% models, thus indicating the differentiation of HDFn into myofibroblasts. It is believed that the interplay between cells and the collagen matrix can induce this effect. HDFn reorganize and align the collagen fibrils parallel to the mandrel, thereby contracting the matrix and generating mechanical stress⁹⁷. This environment is sensed by the cells, which begin to differentiate into myofibroblasts and to remodel the ECM⁹⁸ by *de-novo* expression of stress fibers and adhesion complexes⁹⁹. Positively, this adaptive process that resembles the events occurring during coronary repair¹⁰⁰ may result in cellular and ECM arrangements closer to those found in the native vascular wall.

In summary, the biomimetic character of the ELR and cellularized collagen layers, along with the high versatility of the biocasting technique, in terms of cell type, cell density, layer dimensions and composition, highlights the potential of the technology described herein for the manufacture of novel vascular wall replicas for cardiovascular applications.

Conclusions

A biocasting technique for the manufacture of EEL and tunica adventitia bi-layered models has been developed using an ELR and an HDFn-cellularized collagen layer. The selected click catalyst-free covalent approach, along with the hydrophobically folded state of the ELR matrix at r.t., confers elastic properties to the inner ELR layer while mimicking the wavy morphology found in the native elastic lamina. On the other hand, the cellularized collagen matrix exhibits a more viscous character with a smooth morphology similar to that displayed by the tunica adventitia. Maturation *in vitro* revealed the ability of the cell-adhesive domains, encoded in the ELR sequence, to preserve the cytocompatible character of the collagen model and reverse the HDFn polarization from the outer surface, in contact with the culture medium, to the ELR-collagen interface. Histology studies showed the enhanced expression of ECM components, such as α -SMA, FAK, and acid polysaccharides conforming GAGs and PGs, thus indicating the differentiation of HDFn into myofibroblasts and the cell-remodelling activity over the collagen matrix. The partial substitution of collagen for ELR (30 % by weight) was found to preserve the mechanical and biological features of the bi-layered model, highlighting the versatile character of this biocasting technique for tuning the composition of the layers. This technology may be applicable to the design of novel biomimetic tubular models for the study of vascular wall biomechanics and cardiovascular diseases.

Conflicts of interest

There are no conflicts to declare.

Acknowledgements

The authors are grateful for funding from the Spanish Government (MAT2016-78903-R, RTI2018-096320-B-C22, FPU15-00448 and EST18/00068), the Junta de Castilla y León (VA317P18), the Interreg V A España Portugal POCTEP (0624_2IQBIONEURO_6_E), the Centro en Red de Medicina Regenerativa y Terapia Celular de Castilla y León, the Natural Sciences and Engineering Research Council of Canada (NSERC), the NSERC Create Program in Regenerative Medicine, the Canadian Foundation for the Innovation and the Fonds de Recherche du Québec (Nature et Technologies, and Santé).

Notes and references

1. J. E. Bennett, G. A. Stevens, C. D. Mathers, R. Bonita, J. Rehm, M. E. Kruk, L. M. Riley, K. Dain, A. P. Kengne, K. Chalkidou, J. Beagley, S. P. Kishore, W. Chen, S. Saxena, D. W. Bettcher, J. T. Grove, R. Beaglehole and M. Ezzati, *The Lancet*, 2018, **392**, 1072-1088.
2. S. S. Virani, A. Alonso, E. J. Benjamin, M. S. Bittencourt, C. W. Callaway, A. P. Carson, A. M. Chamberlain, A. R. Chang, S. Cheng and F. N. Delling, *Circulation*, 2020, **141**, e139-e596.
3. F. Copes, N. Pien, S. Van Vlierberghe, F. Boccafosci and D. Mantovani, *Frontiers in bioengineering and biotechnology*, 2019, **7**, 166-166.
4. H. H. G. Song, R. T. Rumma, C. K. Ozaki, E. R. Edelman and C. S. Chen, *Cell Stem Cell*, 2018, **22**, 340-354.
5. S. Dimitrievska and L. E. Niklason, *Cold Spring Harbor perspectives in medicine*, 2017, a025742.
6. J. E. Wagenseil and R. P. Mecham, *Physiological Reviews*, 2009, **89**, 957-989.
7. J. Xu and G.-P. Shi, *Biochim Biophys Acta*, 2014, **1842**, 2106-2119.
8. R. Mazurek, J. M. Dave, R. R. Chandran, A. Misra, A. Q. Sheikh and D. M. Greif, *Adv Pharmacol*, 2017, **78**, 323-350.
9. J.-M. Bourget, V. Laterreur, R. Gauvin, M. D. Guillemette, C. Miville-Godin, M. Mounier, M. Y. Tondreau, C. Tremblay, R. Labbé, J. Ruel, F. A. Auger, T. Veres and L. Germain, *Journal of Tissue Engineering and Regenerative Medicine*, 2017, **11**, 2479-2489.
10. N. L'Heureux, N. Dusserre, G. König, B. Victor, P. Keire, T. N. Wight, N. A. F. Chronos, A. E. Kyles, C. R. Gregory, G. Hoyt, R. C. Robbins and T. N. McAllister, *Nature Medicine*, 2006, **12**, 361-365.
11. N. L'heureux, S. Pâquet, R. Labbé, L. Germain and F. A. Auger, *The FASEB Journal*, 1998, **12**, 47-56.
12. M. J. W. Koens, K. A. Faraj, R. G. Wismans, J. A. van der Vliet, A. G. Krasznai, V. M. J. I. Cuijpers, J. A. Jansen, W. F. Daamen and T. H. van Kuppevelt, *Acta Biomaterialia*, 2010, **6**, 4666-4674.
13. M. J. McClure, S. A. Sell, D. G. Simpson, B. H. Walpoth and G. L. Bowlin, *Acta Biomaterialia*, 2010, **6**, 2422-2433.
14. M. J. McClure, D. G. Simpson and G. L. Bowlin, *Journal of the Mechanical Behavior of Biomedical Materials*, 2012, **10**, 48-61.
15. C. B. Weinberg and E. Bell, *Science*, 1986, **231**, 397.
16. T. Matsuda and H. Miwa, *The Journal of Thoracic and Cardiovascular Surgery*, 1995, **110**, 988-997.
17. A. Hasan, A. Paul, A. Memic and A. Khademhosseini, *Biomedical Microdevices*, 2015, **17**, 88.
18. S. Sartore, A. Chiavegato, E. Faggin, R. Franch, M. Puato, S. Ausoni and P. Pualetto, *Circulation Research*, 2001, **89**, 1111-1121.
19. B. H. Strauss and M. Rabinovitch, *American Journal of Respiratory Cell and Molecular Biology*, 2000, **22**, 1-3.
20. A. K. Harris, D. Stopak and P. Wild, *Nature*, 1981, **290**, 249-251.
21. N. Rajan, J. Habermehl, M.-F. Coté, C. J. Doillon and D. Mantovani, *Nature Protocols*, 2006, **1**, 2753-2758.
22. K. Maskos and W. Bode, *Molecular Biotechnology*, 2003, **25**, 241-266.
23. A. Page-McCaw, A. J. Ewald and Z. Werb, *Nature Reviews Molecular Cell Biology*, 2007, **8**, 221-233.
24. Y. Nagai, *The Journal of Biochemistry*, 1961, **50**, 486-492.
25. K. M. Pawelec, S. M. Best and R. E. Cameron, *Journal of Materials Chemistry B*, 2016, **4**, 6484-6496.
26. S. Rhee and F. Grinnell, *Advanced Drug Delivery Reviews*, 2007, **59**, 1299-1305.
27. S. Rhee, *Experimental & Molecular Medicine*, 2009, **41**, 858-865.
28. R. Wang, J. Ozsvar, G. C. Yeo and A. S. Weiss, *Current Opinion in Chemical Engineering*, 2019, **24**, 54-60.
29. H. Vindin, S. M. Mithieux and A. S. Weiss, *Matrix Biology*, 2019, **84**, 4-16.

30. J. C. Liu, S. C. Heilshorn and D. A. Tirrell, *Biomacromolecules*, 2004, **5**, 497-504.
31. M. Pierna, M. Santos, F. J. Arias, M. Alonso and J. C. Rodríguez-Cabello, *Biomacromolecules*, 2013, **14**, 1893-1903.
32. T. Flora, I. González de Torre, M. Alonso and J. C. Rodríguez-Cabello, *Biofabrication*, 2019, **11**, 035008.
33. D. J. Coletta, A. Ibáñez-Fonseca, L. R. Missana, M. V. Jammal, E. J. Vitelli, M. Aimone, F. Zabalza, J. P. M. Issa, M. Alonso and J. C. Rodríguez-Cabello, *Tissue Engineering Part A*, 2017, **23**, 1361-1371.
34. A. Fernández-Colino, F. J. Arias, M. Alonso and J. C. Rodríguez-Cabello, *Biomacromolecules*, 2014, **15**, 3781-3793.
35. S. Salinas-Fernández, M. Santos, M. Alonso, L. Quintanilla and J. C. Rodríguez-Cabello, *Applied Materials Today*, 2019, DOI: <https://doi.org/10.1016/j.apmt.2019.100500>, 100500.
36. C. M. Madl, L. M. Katz and S. C. Heilshorn, *Advanced Functional Materials*, 2016, **26**, 3612-3620.
37. I. González de Torre, M. Santos, L. Quintanilla, A. Testera, M. Alonso and J. C. Rodríguez Cabello, *Acta Biomaterialia*, 2014, **10**, 2495-2505.
38. S. E. D'Souza, M. H. Ginsberg and E. F. Plow, *Trends in Biochemical Sciences*, 1991, **16**, 246-250.
39. S. Meiners and M. L. T. Mercado, *Molecular Neurobiology*, 2003, **27**, 177-195.
40. J.-D. Vassalli, A. Sappino and D. Belin, *The Journal of clinical investigation*, 1991, **88**, 1067-1072.
41. K. S. Straley and S. C. Heilshorn, *Advanced Materials*, 2009, **21**, 4148-4152.
42. A. M. Testera, A. Girotti, I. G. de Torre, L. Quintanilla, M. Santos, M. Alonso and J. C. Rodríguez-Cabello, *Journal of Materials Science: Materials in Medicine*, 2015, **26**, 105.
43. R. R. Costa, C. A. Custódio, F. J. Arias, J. C. Rodríguez-Cabello and J. F. Mano, *Small*, 2011, **7**, 2640-2649.
44. S. S. Amruthwar, A. D. Puckett and A. V. Janorkar, *Journal of Biomedical Materials Research Part A*, 2013, **101A**, 2383-2391.
45. S. Meghezi, D. G. Seifu, N. Bono, L. Unsworth, K. Mequanint and D. Mantovani, *Jove-Journal of Visualized Experiments*, 2015, DOI: 10.3791/52812, 52812.
46. C. Loy, A. Lainé and D. Mantovani, *Biotechnology Journal*, 2016, **11**, 1673-1679.
47. M.-J. Chow, R. Turcotte, Charles P. Lin and Y. Zhang, *Biophysical Journal*, 2014, **106**, 2684-2692.
48. A. J. Cocciolone, J. Z. Hawes, M. C. Staiculescu, E. O. Johnson, M. Murshed and J. E. Wagenseil, *American Journal of Physiology-Heart and Circulatory Physiology*, 2018, **315**, H189-H205.
49. K. N. Greenland, M. F. C. A. Carvajal, J. M. Preston, S. Ekblad, W. L. Dean, J. Y. Chiang, R. L. Koder and R. J. Wittebort, *The Journal of Physical Chemistry B*, 2018, **122**, 2725-2736.
50. F. H. Silver, *Journal of Engineered Fibers and Fabrics*, 2009, **4**, 155892500900400203.
51. N. Bono, S. Meghezi, M. Soncini, M. Piola, D. Mantovani and G. B. Fiore, *Annals of Biomedical Engineering*, 2017, **45**, 1496-1510.
52. P. Fernandez and A. R. Bausch, *Integrative Biology*, 2009, **1**, 252-259.
53. K. Lin, D. Zhang, M. H. Macedo, W. Cui, B. Sarmento and G. Shen, *Advanced Functional Materials*, 2019, **29**, 1804943.
54. J. P. E. Junker, P. Sommar, M. Skog, H. Johnson and G. Kratz, *Cells Tissues Organs*, 2010, **191**, 105-118.
55. A. Suehiro, S. Hirano, Y. Kishimoto, B. Rousseau, T. Nakamura and J. Ito, *Acta Oto-Laryngologica*, 2010, **130**, 844-850.
56. M. A. Traore and S. C. George, *Tissue Engineering Part B: Reviews*, 2017, **23**, 505-514.
57. L. D. Muiznieks, S. Sharpe, R. Pomès and F. W. Keeley, *Journal of Molecular Biology*, 2018, **430**, 4741-4753.
58. P. Fratzl, K. Misof, I. Zizak, G. Rapp, H. Amenitsch and S. Bernstorff, *Journal of structural biology*, 1998, **122**, 119-122.
59. B. Brodsky and A. V. Persikov, in *Advances in protein chemistry*, Elsevier, 2005, vol. 70, pp. 301-339.
60. N. K. Li, F. G. Quiroz, C. K. Hall, A. Chilkoti and Y. G. Yingling, *Biomacromolecules*, 2014, **15**, 3522-3530.
61. A. Patel, B. Fine, M. Sandig and K. Mequanint, *Cardiovascular Research*, 2006, **71**, 40-49.
62. C. Guidry and F. Grinnell, *Collagen and Related Research*, 1987, **6**, 515-529.
63. A. Nieponice, L. Soletti, J. Guan, Y. Hong, B. Gharaibeh, T. M. Maul, J. Huard, W. R. Wagner and D. A. Vorp, *Tissue Engineering Part A*, 2010, **16**, 1215-1223.
64. C. Loy, D. Pezzoli, G. Candiani and D. Mantovani, *Biotechnology Journal*, 2018, **13**, 1700359.
65. D. I. Shreiber, V. H. Barocas and R. T. Tranquillo, *Biophysical journal*, 2003, **84**, 4102-4114.
66. M. E. Ita and B. A. Winkelstein, *Journal of Biomechanical Engineering*, 2019, **141**.
67. S.-W. Chang, B. P. Flynn, J. W. Ruberti and M. J. Buehler, *Biomaterials*, 2012, **33**, 3852-3859.
68. J. Yang, R. Bai, B. Chen and Z. Suo, *Advanced Functional Materials*, 2020, **30**, 1901693.
69. J. Yang, R. Bai and Z. Suo, *Advanced Materials*, 2018, **30**, 1800671.
70. R. S. Erdmann and H. Wennemers, *Journal of the American Chemical Society*, 2010, **132**, 13957-13959.
71. H. J. Lee, G. M. Fernandes-Cunha, K.-S. Na, S. M. Hull and D. Myung, *Advanced Healthcare Materials*, 2018, **7**, 1800560.
72. T. V. How, in *Cardiovascular Biomaterials*, ed. G. W. Hastings, Springer London, London, 1992, DOI: 10.1007/978-1-4471-1847-3_1, pp. 1-35.
73. C. Loy, S. Meghezi, L. Lévesque, D. Pezzoli, H. Kumra, D. Reinhardt, J. N. Kizhakkedathu and D. Mantovani, *Biomaterials Science*, 2017, **5**, 153-162.
74. D. B. Camasão, M. González-Pérez, S. Palladino, M. Alonso, J. C. Rodríguez-Cabello and D. Mantovani, *Biomaterials Science*, 2020, DOI: 10.1039/D0BM00292E.
75. R. Gauvin, T. Ahsan, D. Larouche, P. Lévesque, J. Dubé, F. A. Auger, R. M. Nerem and L. Germain, *Tissue Engineering Part A*, 2010, **16**, 1737-1747.
76. A. J. Schriebl, T. Schmidt, D. Balzani, G. Sommer and G. A. Holzapfel, *Acta Biomaterialia*, 2015, **17**, 125-136.
77. I. Vesely, *Journal of Biomechanics*, 1997, **31**, 115-123.
78. D. Pezzoli, J. Di Paolo, H. Kumra, G. Fois, G. Candiani, D. P. Reinhardt and D. Mantovani, *Biomaterials*, 2018, **180**, 130-142.

79. A. Tajaddini, D. L. Kilpatrick, P. Schoenhagen, E. M. Tuzcu, M. Lieber and D. G. Vince, *American Journal of Physiology-Heart and Circulatory Physiology*, 2005, **288**, H250-H255.
80. A. Karimi, M. Navidbakhsh, A. Shojaei and S. Faghihi, *Materials Science and Engineering: C*, 2013, **33**, 2550-2554.
81. I. Ozolanta, G. Tetere, B. Purinya and V. Kasyanov, *Medical Engineering & Physics*, 1998, **20**, 523-533.
82. D. B. Camasão, D. Pezzoli, C. Loy, H. Kumra, L. Levesque, D. P. Reinhardt, G. Candiani and D. Mantovani, *Biotechnology Journal*, 2019, **14**, 1700768.
83. E. M. Green, J. C. Mansfield, J. S. Bell and C. P. Winlove, *Interface Focus*, 2014, **4**, 20130058.
84. R. P. Mecham and J. E. Heuser, in *Cell Biology of Extracellular Matrix: Second Edition*, ed. E. D. Hay, Springer US, Boston, MA, 1991, DOI: 10.1007/978-1-4615-3770-0_4, pp. 79-109.
85. J. Schöneberg, F. De Lorenzi, B. Theek, A. Blaeser, D. Rommel, A. J. C. Kuehne, F. Kießling and H. Fischer, *Scientific Reports*, 2018, **8**, 10430.
86. Z. Chen, M. Tang, D. Huang, W. Jiang, M. Li, H. Ji, J. Park, B. Xu, L. J. Atchison, G. A. Truskey and K. W. Leong, *Lab on a Chip*, 2018, **18**, 2047-2054.
87. J. Robert, B. Weber, L. Frese, M. Y. Emmert, D. Schmidt, A. von Eckardstein, L. Rohrer and S. P. Hoerstrup, *PLOS ONE*, 2013, **8**, e79821.
88. D. C. O. Thornton, E. M. Fejes, S. F. DiMarco and K. M. Clancy, *Limnology and Oceanography: Methods*, 2007, **5**, 73-87.
89. A. D. Theocharis, S. S. Skandalis, C. Gialeli and N. K. Karamanos, *Advanced Drug Delivery Reviews*, 2016, **97**, 4-27.
90. R. V. Iozzo and L. Schaefer, *Matrix Biology*, 2015, **42**, 11-55.
91. T. Horigome, S. Takumi, K. Shirai, T. Kido, N. Hagiwara-Chatani, A. Nakashima, N. Adachi, H. Yano and Y. Hirai, *Journal of Dermatological Science*, 2017, **86**, 132-141.
92. S. W. Van Den Borne, J. Diez, W. M. Blankesteijn, J. Verjans, L. Hofstra and J. Narula, *Nature Reviews Cardiology*, 2010, **7**, 30.
93. B. Hinz, C. A. McCulloch and N. M. Coelho, *Experimental Cell Research*, 2019, **379**, 119-128.
94. B. Hinz, V. Dugina, C. Ballestrem, B. Wehrle-Haller and C. Chaponnier, *Molecular Biology of the Cell*, 2003, **14**, 2508-2519.
95. H.-B. Wang, M. Dembo, S. K. Hanks and Y.-I. Wang, *Proceedings of the National Academy of Sciences*, 2001, **98**, 11295.
96. X.-K. Zhao, Y. Cheng, M. Liang Cheng, L. Yu, M. Mu, H. Li, Y. Liu, B. Zhang, Y. Yao, H. Guo, R. Wang and Q. Zhang, *Scientific Reports*, 2016, **6**, 19276.
97. B. Hinz and G. Gabbiani, *Current Opinion in Biotechnology*, 2003, **14**, 538-546.
98. N. Sandbo and N. Dulin, *Translational Research*, 2011, **158**, 181-196.
99. J. J. Tomasek, G. Gabbiani, B. Hinz, C. Chaponnier and R. A. Brown, *Nature Reviews Molecular Cell Biology*, 2002, **3**, 349-363.
100. M. Coen, G. Gabbiani, M.-L. Bochaton-Piallat and Y. E. Chen, *Arteriosclerosis, Thrombosis, and Vascular Biology*, 2011, **31**, 2391-2396.